PET Imaging of VEGFR-2 Expression in Lung Cancer with ^{64}Cu-Labeled Ramucirumab

Haiming Luo*[1], Christopher G. England*[2], Stephen A. Graves[2], Haiyan Sun[1], Glenn Liu[3], Robert J. Nickles[2], and Weibo Cai[1–3]

[1]*Department of Radiology, University of Wisconsin–Madison, Madison, Wisconsin;* [2]*Department of Medical Physics, University of Wisconsin–Madison, Madison, Wisconsin; and* [3]*University of Wisconsin Carbone Cancer Center, Madison, Wisconsin*

Lung cancer accounts for 17% of cancer-related deaths worldwide, and most patients present with locally advanced or metastatic disease. Novel PET imaging agents for assessing vascular endothelial growth factor receptor-2 (VEGFR-2) expression can be used for detecting VEGFR-2–positive malignancies and subsequent monitoring of therapeutic response to VEGFR-2–targeted therapies. Here, we report the synthesis and characterization of an antibody-based imaging agent for PET imaging of VEGFR-2 expression in vivo. **Methods:** Ramucirumab (named RamAb), a fully humanized IgG1 monoclonal antibody, was conjugated to 2-*S*-(4-isothiocyanatobenzyl)-1,4,7-triazacyclononane-1,4,7-triacetic acid (p-SCN-Bn-NOTA) and labeled with ^{64}Cu. Flow cytometry analysis and microscopy studies were performed to compare the VEGFR-2 binding affinity of RamAb and NOTA-RamAb. PET imaging and biodistribution studies were performed in nude mice bearing HCC4006 and A549 xenograft tumors. Ex vivo histopathology was performed to elucidate the expression patterns of VEGFR-2 in different tissues and organs to validate in vivo results. **Results:** Flow cytometry examination revealed the specific binding capacity of fluorescein isothiocyanate-RamAb to VEGFR-2, and no difference in VEGFR-2 binding affinity was seen between RamAb and NOTA-RamAb. After being labeled with ^{64}Cu, PET imaging revealed specific and prominent uptake of ^{64}Cu-NOTA-RamAb in VEGFR-2–positive HCC4006 tumors (9.4 ± 0.5 percentage injected dose per gram at 48 h after injection; $n = 4$) and significantly lower uptake in VEGFR-2–negative A549 tumors (4.3 ± 0.2 percentage injected dose per gram at 48 h after injection; $n = 3$). Blocking experiments revealed significantly lower uptake in HCC4006 tumors, along with histology analysis, further confirming the VEGFR-2 specificity of ^{64}Cu-NOTA-RamAb. **Conclusion:** This study provides initial evidence that ^{64}Cu-NOTA-RamAb can function as a PET imaging agent for visualizing VEGFR-2 expression in vivo, which may also find potential applications in monitoring the treatment response of VEGFR-2–targeted cancer therapy.

Key Words: vascular endothelial growth factor receptor-2 (VEGFR-2); ramucirumab; positron emission tomography (PET); ^{64}Cu; molecular imaging

J Nucl Med 2016; 57:285–290
DOI: 10.2967/jnumed.115.166462

Despite significant advances in the treatment of many malignancies, lung cancer remains the leading cause of cancer-related death worldwide, accounting for nearly 17% of all cancer-related deaths (*1*). The average 5-y survival rate for all stages of lung cancer remains critically low at 17%, which has been attributed to insufficient early detection in asymptomatic patients (*2,3*). As therapeutic intervention is highly dependent on early diagnoses and efficient tumor staging, there is a vital need for the development of novel imaging agents. Although CT has been extensively used for preoperative evaluation of lung malignancies (e.g., size, location, disease progression), the low reliability for lymph node staging often limits its usage in determining tumor stage and grade (*4*). In comparison, PET with ^{18}F-FDG can enhance diagnostic accuracy by allowing for effortless discernment between benign and malignant lesions, while also improving identification of nodal metastasis (*5,6*). Although ^{18}F-FDG is a commonly used PET tracer, it displays limited sensitivity and specificity for cancer diagnostics, resulting from the increased metabolism of glucose in several pathologic diseases, including inflammation and infection (*7*).

Angiogenesis inhibitors have been used for the treatment of several cancers, including non–small cell lung cancer (NSCLC), with an emphasis on limiting the proangiogenic effects of vascular endothelial growth factor (VEGF) (*8*). A primary receptor for VEGF, known as vascular endothelial growth factor receptor 2 (VEGFR-2), is a type II transmembrane tyrosine kinase receptor expressed on cancer cells, endothelial cells, and circulating bone marrow–derived endothelial progenitor cells (*9*). The receptor is known to mediate VEGF-induced microvascular permeability, endothelial cell proliferation, and the effects of cellular invasion (*10*). Also, VEGFR-2–mediated neovascularization facilitates the maintenance of normal lung structure and function with inhibition of VEGFR-2 signaling, resulting in decreased lung alveolarization and arterial density (*11*).

Overexpression of VEGFR-2 is associated with tumor progression and poor prognosis in several cancers, making it an attractive marker for VEGFR-2–targeted diagnostic imaging (*12*). Direct imaging of VEGFR-2 would be particularly valuable for tracking patient response to angiogenesis inhibitors, allowing for the monitoring of disease progression (*13*). However, highly sensitive screening modalities are needed to image VEGFR-2 expression, as the receptor presence is limited to the endothelium of vasculature. Several SPECT imaging agents, such as ^{123}I-VEGF$_{165}$, ^{99m}Tc-VEGF$_{121}$, and ^{111}In-hnTf-VEGF, have shown limited success for imaging VEGFR-2 in vivo (*14*). ^{64}Cu-labeled VEGF$_{121}$ was successfully used in the dynamic monitoring of VEGFR-1 and VEGFR-2 receptor expression in numerous disease models, including solid tumors, myocardial

Received Sep. 1, 2015; revision accepted Oct. 21, 2015.
For correspondence or reprints contact: Weibo Cai, Department of Radiology, University of Wisconsin–Madison, Rm. 7137, 1111 Highland Ave., Madison, WI 53705-2275.
E-mail: wcai@uwhealth.org
*Contributed equally to this work.
Published online Nov. 5, 2015.

infarction, and murine hindlimb ischemia (*15*). Wang et al. developed a mutated $VEGF_{121}$ ($VEGF_{DEE}$) for increased VEGFR-2 specificity, yet the challenging synthesis procedures and low tumor signal (~3–5 percentage injected dose per gram [%ID/g]) limited its potential applications (*14*). Ramucirumab (RamAb), also known as IMC-1121B, is a fully humanized IgG1 monoclonal antibody that selectively blocks VEGFR-2 signaling (*16*). Both preclinical and clinical studies have demonstrated the promising efficacy of RamAb for the treatment of various malignancies, including hepatocellular, colorectal, gastric, and lung cancers (*17*). Effective imaging of VEGFR-2 in patients would promote enhanced patient stratification, which may allow physicians to monitor the efficacy of anti–VEGFR-2 therapies in the future.

Herein, we developed a novel PET tracer for the imaging of VEGFR-2 expression in lung cancer using the Food and Drug Administration–approved antibody RamAb. To accomplish this task, RamAb was chelated and radiolabeled with ^{64}Cu (^{64}Cu-NOTA-RamAb) to investigate its biodistribution and VEGFR-2 targeting efficacy in vivo. Two human NSCLC cell lines were selected on the basis of their relative expression levels of VEGFR-2. High levels of VEGFR-2 expression were previously reported in HCC4006 cells, whereas the A549 cell line is known to have low expression levels (*18*). Region-of-interest analysis of PET images was performed for the quantification of ^{64}Cu-NOTA-RamAb uptake and distribution in major tissues/organs. Furthermore, histologic evaluation was performed to confirm that uptake of ^{64}Cu-NOTA-RamAb in tumors was dependent on VEGFR-2 expression levels.

MATERIALS AND METHODS

Chemicals

RamAb was obtained commercially. AlexaFluor488- and Cy3-labeled secondary antibodies were purchased from Jackson ImmunoResearch Laboratories, Inc. NHS-Fluorescein was obtained from Thermo Fisher Scientific. 2-*S*-(4-isothiocyanatobenzyl)-1,4,7-triazacyclononane-1,4,7-triacetic acid (p-SCN-Bn-NOTA) was acquired from Macrocyclics, Inc. PD-10 columns were obtained from GE Healthcare. All other reaction buffers and chemicals used in this study were from Thermo Fisher Scientific.

Cell Lines and Animal Model

Human NSCLC cell lines HCC4006 and A549 and human umbilical vein endothelial cells (HUVECs) were obtained from the American Type Culture Collection. NSCLC cell lines were grown in 5% CO_2 at 37°C in RPMI 1640 medium with high glucose, supplemented with 10% fetal bovine serum. HUVECs were cultured in 5% CO_2 at 37°C in Medium 200, supplemented with low serum growth supplement (Thermo Fisher Scientific). Cells were used for in vitro and in vivo experiments after they reached 60%–70% confluence. All animal studies were conducted under an Institutional Animal Care and Use Committee protocol approved by the University of Wisconsin Institutional Animal Care and Use Committee. For implantation, 5×10^6 tumor cells, mixed at 1:1 with phosphate-buffered saline (PBS) and Matrigel (BD Biosciences), were subcutaneously injected into the front flank of 4- to 5-wk-old female athymic nude mice. Tumor diameter was monitored for 3–5 wk after implantation, and mice with tumors between 5 and 8 mm were used for in vivo experiments.

NOTA/Fluorescein Isothiocyanate (FITC) Conjugation and ^{64}Cu Labeling of RamAb

The conjugation of the radioisotope chelator NOTA to RamAb was accomplished using a protocol previously described (*19*). Briefly, a 10:1 ratio of p-SCN-Bn-NOTA and RamAb were incubated together at pH 9.0 at 25°C for 2 h. Similar reaction conditions were performed for the conjugation of RamAb with NHS-Fluorescein. In short, NHS-Fluorescein and RamAb were incubated together at a ratio of 5:1 and allowed to react at 25°C for 2 h. Radioisotopes were produced by a PETrace cyclotron (GE Healthcare) using the ^{64}Ni(p,n)^{64}Cu reaction. ^{64}Cu labeling and purification followed the routine protocol previously described (*20*). Briefly, $^{64}CuCl_2$ (37 MBq) was diluted in 300 μL of 0.1 M sodium acetate buffer (pH 6.5) and added to 20 μg of NOTA-RamAb. The reaction mixture was incubated for 30 min at 37°C with constant shaking. Purification of ^{64}Cu-NOTA-RamAb from free NOTA was accomplished using PD-10 columns with PBS as the mobile phase.

Confocal Imaging and Flow Cytometry

HUVEC and A549 cells were separately seeded into 8-well cover glass bottom chambers (Lab-Tek II Chambered Coverglass; Thermo Scientific) for confocal microscopy. To each chamber well, 10 nM of RamAb were added with cell medium at 25°C for 1 h. After incubation with AlexaFluor488-labeled goat antihuman IgG (2.5 μg/mL) for 4 h at 25°C, cells were washed and analyzed with an A1R confocal microscope (Nikon).

Flow cytometry analysis was used to evaluate the biologic activity of RamAb. Briefly, HUVEC and A549 cells were harvested and suspended in PBS with 2% bovine serum albumin at a concentration of 5×10^6 cells/mL. Cells were incubated with 50 μM FITC-RamAb and FITC-NOTA-RamAb for 1 h at room temperature, washed 3 times with PBS, and centrifuged at 1,000 rpm for 5 min. Cells were washed with PBS and analyzed with a FACSCalibur 4-color analysis cytometer (Becton-Dickinson); data analysis was accomplished using FlowJo software (Three Star, Inc.).

PET Imaging and Biodistribution Studies

PET imaging and data analysis were performed using the microPET/micro-CT Inveon rodent model scanner (Siemens Medical Solutions USA, Inc.) as previously described (*21,22*). Each tumor-bearing mouse was intravenously injected with 5–10 MBq of ^{64}Cu-NOTA-RamAb, and static PET scans were obtained at 3, 24, and 48 h after injection. Tracer uptake was reported as the %ID/g (mean ± SD; ≥ 3 mice per group).

Receptor blocking studies were performed to evaluate the specificity of ^{64}Cu-NOTA-RamAb to VEGFR-2 in vivo. Briefly, 3 mice were each injected with 5–10 MBq of ^{64}Cu-NOTA-RamAb 24 h after the administration of a blocking dose (50 mg/kg) of RamAb. At the last time point (48 h), biodistribution studies were performed to validate the PET data. Radioactivity in tissues and organs was measured using a γ-counter (PerkinElmer).

Histology

Histologic sections of tissue samples were provided by the University of Wisconsin Carbone Cancer Center Experimental Pathology Laboratory. Frozen tissue slices of 5-μm thickness were fixed with cold acetone for 10 min and dried in the air for 30 min. After being rinsed with PBS and blocked with 10% donkey serum for 30 min at 25°C, slices were incubated with 10 nM FITC-RamAb for 6 h at 4°C. After being washed with PBS, tissue slices were stained with rat antimouse CD31 antibody (2 μg/mL) for 4 h at 4°C, followed by Cy3-labeled donkey antirat IgG for 2 h at 25°C. A coverslip was applied to each slide using Vectashield mounting medium for fluorescence microscopy with DAPI (4′,6-diamidino-2-phenylindole) (Vector Laboratories, Inc.). All images were acquired using an A1R confocal microscope (Nikon).

Statistical Analysis

Quantitative data were expressed as mean ± SD. Means were compared using the Student *t* test, with *P* values of less than 0.05 considered statistically significant.

RESULTS

Evaluation of Binding Affinity of RamAb to VEGFR-2

Confocal imaging was used to validate the specific binding of RamAb to VEGFR-2 using a cell line known to express high basal

levels of VEGFR-2, HUVECs, and a cell line that expresses minimal VEGFR-2, A549. As a control, DAPI was used to stain the nucleus of cells. Confocal imaging verified the high expression of VEGFR-2 in HUVECs, as depicted in the green channel. A slightly positive signal in the green channel is visible for the A549 cells, suggesting that VEGFR-2 was expressed at lower levels in this cell line (Fig. 1A).

Binding and uptake of RamAb by VEGFR-2 was further confirmed using flow cytometry (Fig. 1B). Both VEGFR-2–positive cells (HUVEC) and VEGFR-2–negative cells (A549) were incubated with FITC-RamAb to ensure minimal nonspecific binding. A significant shift in FITC intensity is evident between the control (black) and FITC-RamAb (red) samples. Also, blocking of VEGFR-2 in HUVECs resulted in a shift toward the control group, suggesting that blocking effectively decreased the binding and uptake of FITC-RamAb. Additionally, there were no observable differences in cellular uptake between FITC-RamAb (red) and the chelated form, FITC-NOTA-RamAb (green). For comparison, A549 cells showed no shift in fluorescence intensity between the control (black) and FITC-RamAb (red) samples, further proving that RamAb does not undergo nonspecific binding and cellular uptake. Also, decreased RamAb uptake by A549 cells further confirmed that NOTA conjugation did not compromise the binding affinity or specificity of RamAb for VEGFR-2.

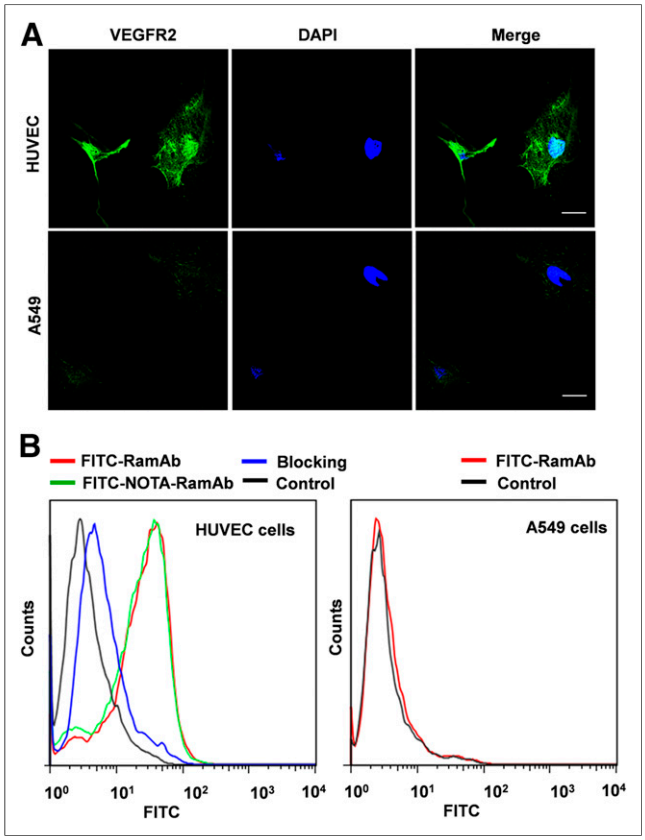

FIGURE 1. Evaluation of binding specificity of FITC-RamAb to VEGFR-2. (A) Assessment of RamAb binding to VEGFR-2–positive HUVEC and VEGFR-2–negative A549 cells by confocal imaging. RamAb was incubated with selected cells, followed by AlexaFluor488-labeled goat antihuman IgG for confocal imaging analysis. Scale bar, 30 μm. (B) VEGFR-2 expression was further evaluated using flow cytometry, revealing large shift in fluorescence intensity for HUVEC cells as compared with A549 cells. Additionally, conjugation of RamAb to NOTA did not affect binding affinity of antibody in HUVEC cells (green).

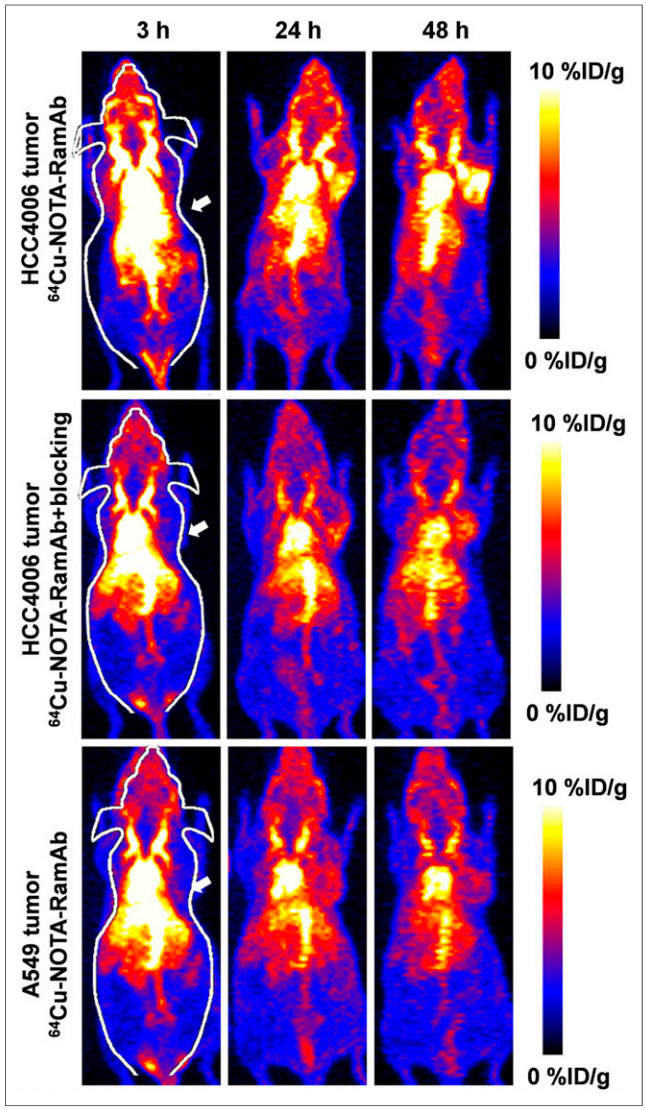

FIGURE 2. PET imaging of VEGFR-2 expression in HCC4006 and A549 tumor–bearing mice. PET maximum-intensity-projection images at 3, 24, and 48 h after injection of ^{64}Cu-NOTA-RamAb or RamAb blocking before ^{64}Cu-NOTA-RamAb are shown, and tumors are indicated by arrows. High tumor accumulation is evident within HCC4006 tumors whereas A549 and blocking experiments showed minimal tumor accumulation.

PET and Biodistribution Studies

The time points of 3, 24, and 48 h after injection were chosen for serial PET scans after intravenous injection of ^{64}Cu-NOTA-RamAb into A549 and HCC4006 tumor–bearing mice. Maximum-intensity projections of mice are shown in Figure 2, with corresponding coronal slices of tumor displayed in Supplemental Figure 1. The quantitative data obtained from the analysis of regions of interest are illustrated in Figure 3 and Supplemental Table 1. High expression of VEGFR-2 in HCC4006 tumors led to rapid accumulation of ^{64}Cu-NOTA-RamAb at 3 h after injection, which increased in a time-dependent manner from 3 to 48 h after injection (3.8 ± 0.5, 8.2 ± 0.5, and 9.4 ± 0.5 %ID/g at 3, 24, and 48 h after injection, respectively; $n = 4$; Fig. 3A). Uptake of ^{64}Cu-NOTA-RamAb in the liver was primarily due to hepatic clearance and transchelation of ^{64}Cu and gradually decreased over time. Similarly, radioactivity in the blood pool was highest during initial time points and decreased

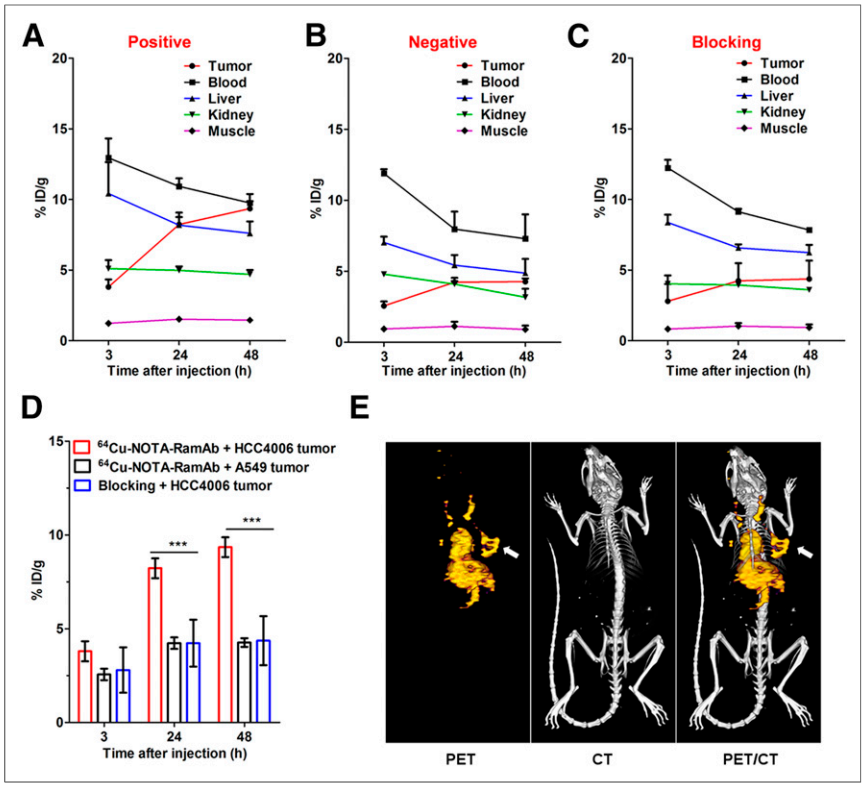

FIGURE 3. Quantitative analysis of PET data. (A) Time–activity curves of HCC4006 tumor, blood, liver, kidney, and muscle on intravenous injection of ^{64}Cu-NOTA-RamAb (n = 3). (B) Time–activity curves of A549 tumor, blood, liver, kidney, and muscle on intravenous injection of ^{64}Cu-NOTA-RamAb (n = 3). (C) Time–activity curves of HCC4006 tumor, blood, liver, kidney, and muscle on intravenous injection of ^{64}Cu-NOTA-RamAb with blocking dose of RamAb (n = 3). (D) Comparison of tumor uptake in all 3 groups (n = 3). (E) Representative PET/CT images of ^{64}Cu-NOTA-RamAb in HCC4006 tumor–bearing mice at 48 h after injection.

in a time-dependent manner. These findings were consistent with our previous studies of radiolabeled antibodies. The liver uptake (10.4 ± 2.2, 8.2 ± 0.9, and 7.6 ± 0.8 %ID/g at 3, 24, and 48 h after injection, respectively) and blood radioactivity (13.0 ± 1.4, 10.9 ± 0.6, and 9.8 ± 0.6 %ID/g at 3, 24, and 48 h after injection, respectively; Fig. 3A) were similar to the values obtained in the VEGFR-2–negative tumor models (A549). The radioactivity accumulated in other organs and tissues was minimal, further demonstrating the high specificity of RamAb. In comparison, uptake of ^{64}Cu-NOTA-RamAb in A549 tumors was low (2.6 ± 0.3, 4.2 ± 0.3, and 4.3 ± 0.2 %ID/g at 3, 24, and 48 h after injection, respectively; n = 3; Fig. 3B). These values were significantly lower than those of the VEGFR-2–positive tumors (HCC4006) at each time point ($P < 0.05$), suggesting that VEGFR-2 targeting is the primary factor for the prominent uptake of ^{64}Cu-NOTA-RamAb in HCC4006 tumors.

Administration of a blocking dose of RamAb significantly reduced the tumor uptake of ^{64}Cu-NOTA-RamAb to 2.8 ± 1.2, 4.2 ± 1.3, and 4.4 ± 1.3 %ID/g at 3, 24, and 48 h after injection, respectively (n = 3; $P < 0.05$ at each time point; Figs. 3C and 3D). Liver uptake (8.4 ± 0.6, 6.6 ± 0.3, and 6.2 ± 0.6 %ID/g at 3, 24, and 48 h after injection, respectively; n = 3; Fig. 3C) and blood radioactivity (12.2 ± 0.6, 9.1 ± 0.2, and 7.8 ± 0.1 %ID/g at 3, 24, and 48 h after injection, respectively; n = 3; Fig. 3C) of ^{64}Cu-NOTA-RamAb in the blocking group were comparable to those of mice injected with ^{64}Cu-NOTA-RamAb alone. Overall, tracer uptake in all major organs was similar between the 2 groups, except for the enhanced uptake found in HCC4006 tumors (significantly higher in the former), further confirming the VEGFR-2 specificity of the tracer.

After the terminal PET scans at 24 h after injection, mice were euthanized for biodistribution studies to validate the quantitative tracer uptake values based on PET imaging data. HCC4006 tumor uptake of ^{64}Cu-NOTA-RamAb was 9.5 ± 2.2 %ID/g at 48 h after injection, significantly higher than ^{64}Cu-NOTA-RamAb in the blocking group (2.4 ± 0.8 %ID/g) and ^{64}Cu-NOTA-RamAb in A549 tumor (2.2 ± 0.7 %ID/g) (Fig. 4; Supplemental Table 2). As a result, HCC4006 displayed the highest uptake of ^{64}Cu-NOTA-RamAb, which provided excellent tumor contrast with tumor-to-muscle ratios of 17.7 ± 14.8 (n = 4) at 24 h after injection. Overall, the biodistribution data matched well with PET region-of-interest data, indicating that the quantitative analysis of noninvasive PET scans accurately reflected the biodistribution of a novel imaging tracer in vivo, as well as VEGFR-2 specificity of ^{64}Cu-NOTA-RamAb.

Histologic Analysis of Tissues

Mice were sacrificed before tumors and major organs (e.g., liver, kidney, and muscle) were harvested for VEGFR-2 and VEGFR-1 staining (Fig. 5). Fluorescence from FITC-RamAb was shown to overlay with the tumor cells, depicted in blue (Fig. 5A). In addition, A549 sections showed minimal expression of VEGFR-2 that did not overlay with tumor vasculature (CD31) or cells (DAPI). Blocking of VEGFR-2 effectively resulted in minimal RamAb binding, providing further evidence of RamAb selectivity. This further confirmed that RamAb possesses high binding specificity for VEGFR-2. Additionally, VEGFR-2 staining of mouse liver and kidney displayed low signal, indicating that humanized RamAb antibody does not undergo binding with murine VEGFR-2. Thus, uptake of ^{64}Cu-NOTA-RamAb in the liver can be attributed to hepatic clearance of the tracer, rather than VEGFR-2 binding. VEGFR-1 immunofluorescence staining in A549 and HCC4006 tumors showed that A549 tumor sections expressed significantly higher levels of VEGFR-1 in comparison to HCC4006 (Fig. 5B).

DISCUSSION

VEGFR-2 is a crucial target for several clinical and preclinical antiangiogenic therapies, as it is a significant factor in determining cancer progression. VEGFR-2 actively regulated several factors of angiogenesis, including endothelial cell survival, cell migration, and proliferation of blood vessels; thus, imaging of VEGFR-2 expression is vital for selecting patients who may benefit from antiangiogenic therapies (*23*). Several strategies have been adopted to block the VEGF/VEGFR-2 signaling pathway for cancer treatment, such as the development of novel agents that prevent VEGF-A binding to its receptor (e.g., bevacizumab, VEGF-trap), antibodies that directly

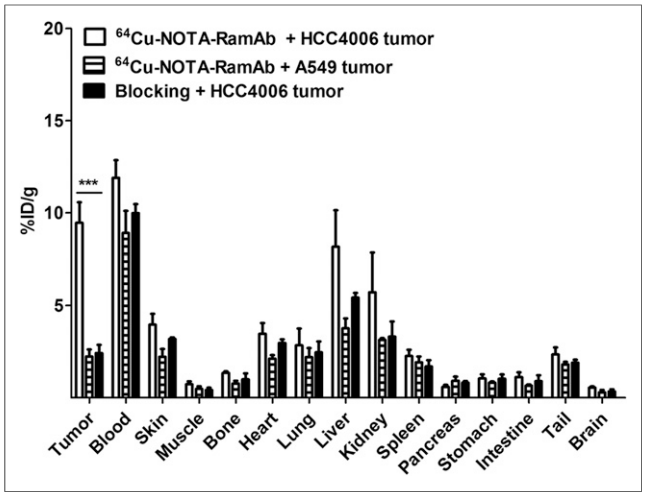

FIGURE 4. Biodistribution of ^{64}Cu-NOTA-RamAb in HCC4006 and A549 tumors as well as ^{64}Cu-NOTA-RamAb with a blocking dose of RamAb in HCC4006 tumors at 48 h after injection. $n = 3$.

block ligand-induced activation of VEGFR-2 (e.g., RamAb, DC101), and small molecules that inhibit the kinase activity of VEGFR-2 (e.g., SU5416, DMH4) (*24*). RamAb was the first human monoclonal antibody approved by the U.S. Food and Drug Administration that specifically targets VEGFR-2 for the treatment of several cancers (*25*). RamAb directly targets the extracellular VEGF-binding domain of VEGFR-2, thus preventing binding of all VEGFR-associated ligands. For comparison, RamAb is more selective than bevacizumab, as the therapeutic action of bevacizumab by blocking of VEGFR-1 and VEGFR-2 activity (*24*).

Noninvasive imaging and quantification of VEGFR-2 expression may provide physicians with needed information for selecting patients who may benefit from receiving therapeutic intervention with antiangiogenic-based therapies in the future. Also, imaging of VEGFR-2 may provide insight into the preclinical development of novel antiangiogenic compounds. Some radiotracers have been previously reported for in vivo imaging of VEGFR expression, including targeting of VEGFR-1 and VEGFR-2 with VEGF-A (*26*). However, VEGF-A tracers face the challenge of high renal uptake, due to high VEGFR-1 expression in the kidney, resulting in low signal contrast and hampered clinical translation (*27*). Although the ^{64}Cu-labeled mutant of $VEGF_{121}$ ($VEGF_{DEE}$) achieved promising results for lowering kidney uptake, accurate evaluation of the dynamic microdistribution of VEGFR-2 in vivo with high spatial and temporal resolution remains a major challenge (*28*).

To our knowledge, this study reports the first instance of using radiolabeled RamAb for the molecular imaging of VEGFR-2 expression in vivo. We successfully developed and characterized ^{64}Cu-NOTA-RamAb for PET imaging of VEGFR-2 expression in NSCLC xenograft tumors. Although the selectivity of RamAb for VEGFR-2 was previously reported in vitro (*29*), we used A549 (VEGFR-2–negative/VEGFR-1–positive) and HCC4006 (VEGFR-2–positive/VEGFR-1–negative) cell lines to further show the selectivity of RamAb for VEGFR-2 (*30,31*). VEGFR-2 specificity of ^{64}Cu-NOTA-RamAb was demonstrated by experiments in vitro, in vivo, and ex vivo, proving it as a promising PET tracer with high clinical potential for diagnosing and monitoring VEGFR-2 expression in tumors. Compared with other antibody-based PET tracers, the tumor accumulation of RamAb obtained in this study is relatively low (~10 %ID/g). The reason for this lower uptake may be that RamAb is targeting a receptor that is expressed at lower levels in comparison to VEGFR-1 (*32*).

The advantages of antibody-based tracers can be attributed to their high binding selectivity for specific receptors or antigens, making them optimal candidates for both drug delivery and molecular imaging. Improvements in tumor accumulation may be obtained through using fragmented RamAb, because antibody fragments display rapid blood clearance in vivo due to their small size. ^{64}Cu has been extensively examined as a potential diagnostic agent, and ^{67}Cu can be a perfect therapeutic isotope that possesses the same chemical entity, which can facilitate future clinical translation, especially when RamAb is already in clinical use (*33*). In future studies, several other isotopes (e.g., ^{89}Zr, ^{52}Mn, and ^{55}Co) display appropriate radioactive decay and emission characteristics suitable for intact antibody-based PET imaging (*34,35*), which could be investigated for potential clinical translation should PET scans at later times (e.g., 3–10 d after injection of radiolabeled RamAb) be needed in cancer patients to evaluate VEGFR-2 expression. One issue that needs to be considered in future clinical investigation is that these isotopes may lead to higher radiation doses to normal organs than ^{64}Cu-labeled antibodies. Also, employment of other disease models may provide new information regarding the role of VEGFR-2 in the progression of other human illnesses.

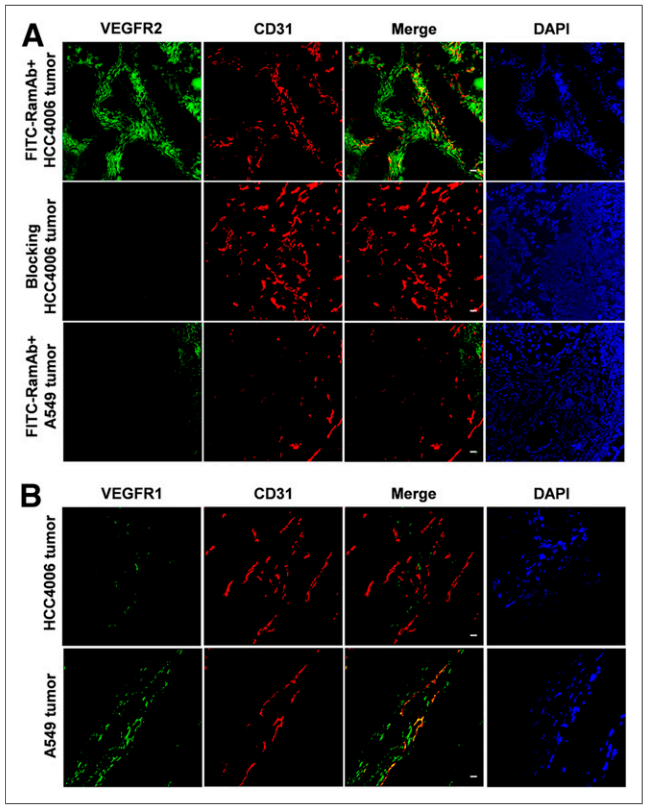

FIGURE 5. Immunofluorescence of VEGFR-2 and VEGFR-1 staining in HCC4006 and A549 tumors and tissue sections. (A) FITC-RamAb was used for VEGFR-2 staining (green). (B) Staining of HCC4006 and A549 tumor sections with an anti–VEGFR-1 antibody (green). Afterward, tissue slices were stained with rat antimouse CD31 antibody and Cy3-labeled donkey antirat IgG (red). DAPI staining was used to reveal location of cell nuclei (blue). Scale bar, 20 μm.

CONCLUSION

Herein, we have successfully investigated ^{64}Cu-NOTA-RamAb for PET imaging of VEGFR-2 expression in NSCLC tumor models. Fast, prominent, and persistent VEGFR-2–specific uptake of ^{64}Cu-NOTA-RamAb in HCC4006 (VEGFR-2–positive) tumors was observed, which was further validated by in vitro experiments. Also, we demonstrated that ^{64}Cu-NOTA-RamAb was specifically binding to VEGFR-2 using a cell line expressing low levels of VEGFR-2 (A549). On further optimization and development, RamAb-based PET tracers may be translated into the clinic for cancer imaging and treatment monitoring in the future.

DISCLOSURE

The costs of publication of this article were defrayed in part by the payment of page charges. Therefore, and solely to indicate this fact, this article is hereby marked "advertisement" in accordance with 18 USC section 1734. This work is supported, in part, by the University of Wisconsin–Madison, the National Institutes of Health (NIBIB/NCI 1R01CA169365, P30CA014520, and T32CA009206), the Department of Defense (W81XWH-11-1-0644), and the American Cancer Society (125246-RSG-13-099-01-CCE). No other potential conflict of interest relevant to this article was reported.

REFERENCES

1. Jemal A, Bray F, Center MM, Ferlay J, Ward E, Forman D. Global cancer statistics. *CA Cancer J Clin.* 2011;61:69–90.
2. Sulu E, Tasolar O, Berk Takir H, Yagci Tuncer L, Karakurt Z, Yilmaz A. Delays in the diagnosis and treatment of non-small-cell lung cancer. *Tumori.* 2011;97:693–697.
3. Ellis PM, Vandermeer R. Delays in the diagnosis of lung cancer. *J Thorac Dis.* 2011;3:183–188.
4. Scott WJ, Gobar LS, Terry JD, Dewan NA, Sunderland JJ. Mediastinal lymph node staging of non-small-cell lung cancer: a prospective comparison of computed tomography and positron emission tomography. *J Thorac Cardiovasc Surg.* 1996;111:642–648.
5. Schrevens L, Lorent N, Dooms C, Vansteenkiste J. The role of PET scan in diagnosis, staging, and management of non-small cell lung cancer. *Oncologist.* 2004;9:633–643.
6. Shim SS, Lee KS, Kim BT, et al. Non-small cell lung cancer: prospective comparison of integrated FDG PET/CT and CT alone for preoperative staging. *Radiology.* 2005;236:1011–1019.
7. Fletcher JW, Djulbegovic B, Soares HP, et al. Recommendations on the use of ^{18}F-FDG PET in oncology. *J Nucl Med.* 2008;49:480–508.
8. Gridelli C, Rossi A, Maione P. New antiangiogenetic agents and non-small cell lung cancer. *Crit Rev Oncol Hematol.* 2006;60:76–86.
9. Smith NR, Baker D, James NH, et al. Vascular endothelial growth factor receptors VEGFR-2 and VEGFR-3 are localized primarily to the vasculature in human primary solid cancers. *Clin Cancer Res.* 2010;16:3548–3561.
10. Hicklin DJ, Ellis LM. Role of the vascular endothelial growth factor pathway in tumor growth and angiogenesis. *J Clin Oncol.* 2005;23:1011–1027.
11. Edirisinghe I, Yang SR, Yao H, et al. VEGFR-2 inhibition augments cigarette smoke-induced oxidative stress and inflammatory responses leading to endothelial dysfunction. *FASEB J.* 2008;22:2297–2310.
12. Pajares MJ, Agorreta J, Larrayoz M, et al. Expression of tumor-derived vascular endothelial growth factor and its receptors is associated with outcome in early squamous cell carcinoma of the lung. *J Clin Oncol.* 2012;30:1129–1136.
13. Willmann JK, Paulmurugan R, Chen K, et al. US imaging of tumor angiogenesis with microbubbles targeted to vascular endothelial growth factor receptor type 2 in mice. *Radiology.* 2008;246:508–518.
14. Wang H, Cai W, Chen K, et al. A new PET tracer specific for vascular endothelial growth factor receptor 2. *Eur J Nucl Med Mol Imaging.* 2007;34:2001–2010.
15. Rodriguez-Porcel M, Cai W, Gheysens O, et al. Imaging of VEGF receptor in a rat myocardial infarction model using PET. *J Nucl Med.* 2008;49:667–673.
16. Spratlin JL, Mulder KE, Mackey JR. Ramucirumab (IMC-1121B): a novel attack on angiogenesis. *Future Oncol.* 2010;6:1085–1094.
17. Clarke JM, Hurwitz HI. Targeted inhibition of VEGF receptor 2: an update on ramucirumab. *Expert Opin Biol Ther.* 2013;13:1187–1196.
18. Riquelme E, Suraokar M, Behrens C, et al. VEGF/VEGFR-2 upregulates EZH2 expression in lung adenocarcinoma cells and EZH2 depletion enhances the response to platinum-based and VEGFR-2-targeted therapy. *Clin Cancer Res.* 2014;20:3849–3861.
19. Hong H, Zhang Y, Nayak TR, et al. Immuno-PET of tissue factor in pancreatic cancer. *J Nucl Med.* 2012;53:1748–1754.
20. Luo H, Hong H, Slater MR, et al. PET of c-Met in cancer with ^{64}Cu-labeled hepatocyte growth factor. *J Nucl Med.* 2015;56:758–763.
21. Zhang Y, Hong H, Engle JW, Yang Y, Barnhart TE, Cai W. Positron emission tomography and near-infrared fluorescence imaging of vascular endothelial growth factor with dual-labeled bevacizumab. *Am J Nucl Med Mol Imaging.* 2012;2:1–13.
22. Hong H, Severin GW, Yang Y, et al. Positron emission tomography imaging of CD105 expression with ^{89}Zr-Df-TRC105. *Eur J Nucl Med Mol Imaging.* 2012;39:138–148.
23. Baeriswyl V, Christofori G. The angiogenic switch in carcinogenesis. *Semin Cancer Biol.* 2009;19:329–337.
24. Sullivan LA, Brekken RA. The VEGF family in cancer and antibody-based strategies for their inhibition. *MAbs.* 2010;2:165–175.
25. Fontanella C, Ongaro E, Bolzonello S, Guardascione M, Fasola G, Aprile G. Clinical advances in the development of novel VEGFR2 inhibitors. *Ann Transl Med.* 2014;2:123.
26. Zhang Y, Hong H, Niu G, et al. Positron emission tomography imaging of vascular endothelial growth factor receptor expression with ^{61}Cu-labeled lysine-tagged VEGF121. *Mol Pharm.* 2012;9:3586–3594.
27. Cai W, Chen K, Mohamedali KA, et al. PET of vascular endothelial growth factor receptor expression. *J Nucl Med.* 2006;47:2048–2056.
28. Chen F, Zhang Y, Cai W. Molecular MRI of VEGFR-2 reveals intra-tumor and inter-tumor heterogeneity. *Am J Nucl Med Mol Imaging.* 2013;3:312–316.
29. Aprile G, Bonotto M, Ongaro E, Pozzo C, Giuliani F. Critical appraisal of ramucirumab (IMC-1121B) for cancer treatment: from benchside to clinical use. *Drugs.* 2013;73:2003–2015.
30. Wang W, Ma Y, Li J, et al. Specificity redirection by CAR with human VEGFR-1 affinity endows T lymphocytes with tumor-killing ability and anti-angiogenic potency. *Gene Ther.* 2013;20:970–978.
31. Yao J, Wu X, Zhuang G, et al. Expression of a functional VEGFR-1 in tumor cells is a major determinant of anti-PlGF antibodies efficacy. *Proc Natl Acad Sci USA.* 2011;108:11590–11595.
32. Cudmore MJ, Hewett PW, Ahmad S, et al. The role of heterodimerization between VEGFR-1 and VEGFR-2 in the regulation of endothelial cell homeostasis. *Nat Commun.* 2012;3:972.
33. Grünberg J, Novak-Hofer I, Honer M, et al. In vivo evaluation of ^{177}Lu- and 67/^{64}Cu-labeled recombinant fragments of antibody chCE7 for radioimmunotherapy and PET imaging of L1-CAM-positive tumors. *Clin Cancer Res.* 2005;11:5112–5120.
34. Zhou Y, Baidoo KE, Brechbiel MW. Mapping biological behaviors by application of longer-lived positron emitting radionuclides. *Adv Drug Deliv Rev.* 2013;65:1098–1111.
35. Graves SA, Hernandez R, Fonslet J, et al. Novel preparation methods of ^{52}Mn for immunoPET imaging. *Bioconjug Chem.* 2015;26:2118–2124.